The Astronomical Journal, 166:1 (13pp), 2023 July https://doi.org/10.3847/1538-3881/acd63b

OrbitN: A Symplectic Integrator for Planetary Systems Dominated by a Central Mass—Insight into Long-term Solar System Chaos

Richard E. Zeebe
SOEST, University of Hawaii at Manoa, 1000 Pope Road, MSB 629, Honolulu, HI 96822, USA; orbitN.code@gmail.com, zeebe@soest.hawaii.edu
Received 2023 April 18; revised 2023 May 14; accepted 2023 May 15; published 2023 June 6

Abstract

Reliable studies of the long-term dynamics of planetary systems require numerical integrators that are accurate and fast. The challenge is often formidable because the chaotic nature of many systems requires relative numerical error bounds at or close to machine precision ($\sim 10^{-16}$, double-precision arithmetic); otherwise, numerical chaos may dominate over physical chaos. Currently, the speed/accuracy demands are usually only met by symplectic integrators. For example, the most up-to-date long-term astronomical solutions for the solar system in the past (widely used in, e.g., astrochronology and high-precision geological dating) have been obtained using symplectic integrators. However, the source codes of these integrators are unavailable. Here I present the symplectic integrator `orbitN` (lean version 1.0) with the primary goal of generating accurate and reproducible long-term orbital solutions for near-Keplerian planetary systems (here the solar system) with a dominant mass M_0. Among other features, `orbitN-1.0` includes M_0's quadrupole moment, a lunar contribution, and post-Newtonian corrections (1PN) due to M_0 (fast symplectic implementation). To reduce numerical round-off errors, Kahan compensated summation was implemented. I use `orbitN` to provide insight into the effect of various processes on the long-term chaos in the solar system. Notably, 1PN corrections have the opposite effect on chaoticity/stability on a 100 Myr versus Gyr timescale. For the current application, `orbitN` is about as fast as or faster (factor 1.15–2.6) than comparable integrators, depending on hardware.[1]

Unified Astronomy Thesaurus concepts: N-body simulations (1083); Solar system (1528); Celestial mechanics (211); Orbital theory (1182)

1. Introduction

Trustworthy long-term dynamical studies of planetary systems require accurate and fast numerical integrators. The requirements for accuracy and speed are usually mutually exclusive because numerical algorithms generally have to sacrifice accuracy for speed. The chaotic behavior of many *N*-body systems presents a particularly daunting challenge and can produce misleading results if numerical chaos dominates over physical chaos (e.g., Wisdom & Holman 1992; Rauch & Holman 1999; Hernandez et al. 2022). As a result, the desired error tolerance of numerical integrator schemes is at or close to machine precision, i.e., about 10^{-16} at double-precision floating-point arithmetic. The tool of choice to tackle the problem is usually symplectic integrators, which show favorable performance in terms of speed, as well as conservation of energy and angular momentum (e.g., Wisdom & Holman 1991; Yoshida 1990). One example of highly demanding *N*-body integrations are up-to-date long-term solar system integrations that provide astronomical solutions for the past and are widely used in, for instance, astrochronology and high-precision geological dating (Laskar et al. 2011; Zeebe & Lourens 2019, 2022). In addition to accurate and fast integration of the fundamental dynamical equations for the main solar system bodies, generating adequate astronomical solutions requires proper inclusion of (1) the Sun's quadrupole moment J_2, (2) the effect of the Moon, (3) post-Newtonian corrections from general relativity (GR) (1PN), and (4) a contribution from asteroids. Note that while the effects from J_2 and asteroids may appear negligible, their contributions become critical for astronomical solutions over, e.g., a 50 Myr timescale owing to chaos. The most recent astronomical solutions have been obtained using a higher-order symplectic integrator scheme called SABAC_4 (Laskar et al. 2011) and a second-order symplectic scheme available in the integrator package `HNBody` (Rauch & Hamilton 2002; Zeebe 2017). The executable and source code of the SABA integrators have not been made available for researchers to use (Laskar et al. 2011). Binaries of the `HNBody` package are available, while the source code is unavailable (Rauch & Hamilton 2002).

Alternative symplectic integrator packages with available source code that could potentially be used to generate accurate *N*-body/astronomical solutions include `swift/swifter`, `mercury6`, and `REBOUND` (Levison & Duncan 1994; Duncan et al. 1998; Chambers 1999; Kaufmann 2005; Rein & Tamayo 2015). However, `swift/swifter` and `mercury6` do not provide features such as fast and accurate options to include 1PN corrections, which are critical for the current application. While the `REBOUND/REBOUNDx` package does provide 1PN options (Rein & Liu 2012; Rein & Tamayo 2015; Tamayo et al. 2020), their accuracy or performance turned out to be suboptimal for the current problem (see Section 4.3). In this contribution, I present the symplectic integrator `orbitN` (lean version 1.0) with the primary goal of efficiently generating accurate and reproducible long-term orbital solutions for near-Keplerian planetary systems dominated by a central mass. `orbitN` version 1.0 focuses on hierarchical systems without close encounters but can be extended to

[1] The orbitN source code (C) is available at http://github.com/rezeebe/orbitN.

include additional features in future versions.[2] While the current orbitN application focuses on the solar system, orbitN can generally be applied to planetary systems with a dominant mass. The present solar system integrations with orbitN reveal that 1PN corrections have the opposite effect on chaoticity/stability on a 100 Myr versus Gyr timescale.

2. Hamiltonian Splitting

The core of orbitN's integrator scheme is based on a second-order symplectic map, which is described at length elsewhere and is not repeated here (e.g., Wisdom & Holman 1991; Yoshida 1990; Saha & Tremaine 1994; Mikkola 1997; Chambers 1999; Murray & Dermott 1999; Rein & Tamayo 2015). (Note that recent studies indicate that higher-order symplectic schemes are not necessarily advantageous; Hernandez et al. 2022; Abbot et al. 2023.) A few features deserve attention here, such as the Hamiltonian splitting and mass factors, which are important, for instance, for the implementation of 1PN corrections.

The gravitational N-body Hamiltonian may be split into a Kepler part and Interaction part (e.g., Murray & Dermott 1999; Rein & Tamayo 2015):

$$\mathcal{H} = \mathcal{H}_{\rm Kep} + \mathcal{H}_{\rm Int}, \tag{1}$$

where

$$\mathcal{H}_{\rm Kep} = \sum_{j=1}^{J}\left(\frac{p'^2_j}{2m'_j} - \frac{\mu_j m'_j}{r'_j}\right) \tag{2}$$

and (Rein & Tamayo 2015)

$$\mathcal{H}_{\rm Int} = \sum_{j=1}^{J}\frac{\mu_j m'_j}{r'_j} - \sum_{j=0}^{J-1}\sum_{k=j+1}^{J}\frac{Gm_j m_k}{r_{jk}}, \tag{3}$$

where $J = N-1$ and N is the total number of bodies in the system, including the dominant mass (index 0); p refers to momentum, m to mass, r to distance, e.g., $r_{jk} = |\boldsymbol{x}_k - \boldsymbol{x}_j|$; and G is the gravitational constant in appropriate units. Primes indicate quantities in Jacobi coordinates (for a summary of coordinate choices and operator splitting, see Hernandez & Dehnen 2017). The factor μ_j is given by $\mu_j = G\cdot\sigma_j$, where

$$\sigma_j = \sum_{i=0}^{j} m_i. \tag{4}$$

Importantly, the mass factor in the first term of Equation (3) depends on the Hamiltonian splitting, which differs, for instance, between Rein & Tamayo (2015) and Saha & Tremaine (1994, hereafter ST94). While the Hamiltonian splitting in orbitN follows Rein & Tamayo (2015), the 1PN corrections in orbitN follow ST94. Hence, the μ_j factors that enter the equation for 1PN corrections here are $\mu_j = G\cdot\sigma_j$ (see Section 3.7), and not $\mu_j = G\cdot\sigma_j/\sigma_{j-1}$ as in ST94.

3. Architecture

orbitN's structure consists of basic function sequences, including input (masses m_j, initial positions $\boldsymbol{x}_j^0$, and velocities $\boldsymbol{v}_j^0$), integration (operator application such as Drift and Kick; see below), and output as requested. orbitN is written in C (C99 standard) and intentionally uses standard function calls with (usually) explicitly stated arguments such as $f(\boldsymbol{x}_j, \boldsymbol{v}_j, \ldots)$ to highlight the function's input and output/updated variables. Large data structures (struct in C/C++), which by design often hide the input and output/updated variables, are avoided. Different integration sequences are available in orbitN, including slow, fast, and fast_pn, as explained below.

The core of orbitN's integrator scheme is based on a second-order symplectic map, frequently referred to as a Wisdom–Holman (WH) map (Wisdom & Holman 1991). The time evolution under the Hamiltonian split (a Kepler part and an Interaction part; see Equation (1)) is realized by Drift and Kick operators, $\mathcal{D}(\tau)$ and $\mathcal{K}(\tau)$ (generally functions of $\boldsymbol{x}_j$, $\boldsymbol{v}_j$, ...), where the operator time step argument τ is usually a simple function of the fixed integration time step Δt. orbitN's second-order integrator is based on a Drift-Kick-Drift operator sequence, advancing the state variables $\boldsymbol{x}_j$ and $\boldsymbol{v}_j$ (e.g., Appendix A, Equation (A3)). The operator code sequence slow reads (time step counter $i = 1,\ldots,n_{\rm step}$)

$$\begin{aligned}&\mathcal{D}(\Delta t/2)\circ\mathcal{K}(\Delta t)\circ\mathcal{D}(\Delta t/2)\circ\ \ldots\\ &\quad\circ\,\mathcal{D}(\Delta t/2)\circ\mathcal{K}(\Delta t)\circ\mathcal{D}(\Delta t/2).\end{aligned} \tag{5}$$

Except for the first and final steps, and when output is requested, the interior $\Delta t/2$-Drift steps can be combined into a single step:

$$\begin{aligned}&\mathcal{D}(\Delta t/2)\circ\mathcal{K}(\Delta t)\circ\mathcal{D}(\Delta t)\circ\ \ldots\\ &\quad\circ\,\mathcal{D}(\Delta t)\circ\mathcal{K}(\Delta t)\circ\mathcal{D}(\Delta t/2),\end{aligned} \tag{6}$$

representing the operator code sequence fast. When including 1PN corrections, additional operators are applied (option fast_pn, see Section 3.7). Ignoring initial and final steps, and including Kahan compensated summation (operator $\mathcal{S}$), the fast_pn core sequence, for example, reads

$$\ldots\circ\,\Gamma\mathcal{D}\Gamma(\tau)\circ\mathcal{S}\circ\mathcal{K}(\Delta t)\circ\mathcal{S}\circ\Gamma\mathcal{D}\Gamma(\tau)\circ\ \ldots, \tag{7}$$

where

$$\Gamma\mathcal{D}\Gamma(\tau) = \Gamma(\Delta t/2)\circ\mathcal{S}\circ\mathcal{D}(\Delta t)\circ\mathcal{S}\circ\Gamma(\Delta t/2) \tag{8}$$

and $\mathcal{S} = \mathcal{S}(\boldsymbol{x}_j, \boldsymbol{v}_j, \ldots)$ (for different Kahan summation options, see Section 3.3), and $\Gamma(\tau)$ represents the γ-term of the 1PN Hamiltonian (see Section 3.7).

orbitN version 1.0 uses Gaussian units, i.e., length, time, and mass are expressed in units of au, days, and fractions of M_0, respectively, although this feature can be extended to other sets of units in future versions. Orbital coordinates in orbitN can be output as state vectors $\boldsymbol{x}_j$, $\boldsymbol{v}_j$ or Keplerian elements. However, for accuracy and archiving of results, state vectors are recommended (see Section 3.1). orbitN's source code is provided to the user and compiled on the local machine. orbitN has been tested on Linux and Mac platforms. For example, a full solar system integration over 100 Myr, comprising the planets, Pluto, and 10 asteroids and including M_0's quadrupole moment, a lunar contribution, and 1PN corrections, requires about 16 hr wall-clock time on a 64-bit Linux machine (gcc optimization level 3, Intel i5-10600 @3.30 GHz; see also Section 4.3).

[2] The orbitN source code (C) is available at github.com/rezeebe/orbitN (correspondence to orbitN.code@gmail.com).

3.1. Trigonometric Functions

Trigonometric functions are frequently employed in numerical integrators, including the WH map. For example, the Drift operator may use Gauss's classic f and g functions to advance ($\boldsymbol{x}_j$, $\boldsymbol{v}_j$) (see Section 3.3), which includes numerical sine and cosine evaluations of the eccentric anomaly (e.g., Danby 1988). The problem with numerical evaluations of trigonometric functions is that different compilers and architectures may produce different results for the same operation. The 2019 IEEE-754 Standard for Floating-Point Arithmetic handles trigonometric functions under "Recommended Operations," which are not mandatory requirements (IEEE 2019). As a result, even if floating-point operations on a given platform adhere to the IEEE-754 standard, there is no guarantee that the results of trigonometric operations are identical between different platforms. For example, I tested evaluation of Gauss's f and g functions on various Linux machines (including the same binary) with the same operating system but different hardware, which yielded different results. Although initially close to machine precision, the differences can grow very quickly, e.g., for chaotic systems, which renders the results of such integrations practically irreproducible (Zeebe 2015a, 2015b, 2022). The problem extends to different architectures, compilers, optimization levels, etc.

Ito & Kojima (2005) discussed the unsatisfactory status of trigonometric functions in computer mathematical libraries and reported their communications with computer manufacturers about the issue. As a work-around, Ito & Kojima (2005) suggested optimizing and porting certain mathematical libraries. I unsuccessfully tested several alternative methods, including compiling sine and cosine functions directly from source code and a discretization/Taylor expansion approach using lookup tables of trigonometric functions (Fukushima 1997). Most methods turned out to be cumbersome to implement and showed poor performance. A satisfactory alternative that also showed good performance is based on Stumpff functions (Stumpff 1959), which avoids evaluation of trigonometric functions altogether (see Section 3.2).

Note in this context that because the conversion of orbital coordinates from state vectors $\boldsymbol{x}_j$, $\boldsymbol{v}_j$ to Keplerian elements involves trigonometric functions, state vectors are recommended for output in `orbitN`, for instance, when accuracy is required and for archiving of results (see above). If needed, a separate routine is provided for post-run conversion of state vectors to Keplerian elements. In that case, and if the selected conversion involves the masses of individual bodies, the user is required to provide the original mass/coordinate input file of the run.

3.2. Stumpff and f and g Functions

The Drift operator (also often called Kepler solver) can be formulated using universal variables and Stumpff functions, the particulars of which have been described elsewhere and are not repeated here (Stumpff 1959; Stiefel & Scheifele 1975; Danby 1987, 1988; Mikkola 1997; Mikkola & Aarseth 1998; Mikkola & Innanen 1999; Rein & Tamayo 2015). In the following, a few details are noted that pertain to the implementation of Stumpff functions in `orbitN`, which follows Rein & Tamayo (2015). The f and g functions used with universal variables and Stumpff functions to advance the Kepler drift from time t to $t+\tau$ may be written as

$$f = 1 - \mu G_2/r \quad ; \quad g = \tau - \mu G_3 \tag{9}$$

$$\dot{f} = -\mu G_1/(r \cdot r_\tau) \quad ; \quad \dot{g} = 1 - \mu G_2/r_\tau, \tag{10}$$

where $\mu = \mu_j$ (see Section 2), $r_\tau = r(t+\tau) = r + \chi G_1 + \zeta G_2$, $\chi = \boldsymbol{x} \cdot \boldsymbol{v}$, $\zeta = \mu - \beta r$, and $\beta = 2\mu/r - v^2$. The so-called G-functions are given by

$$G_n(\beta, s) = s^n \cdot c_n(x) \quad ; \quad x = \beta\, s^2, \tag{11}$$

where s is the variable solved for in Kepler's equation in universal variables (Danby 1987, 1988) and the $c_n(x)$ are Stumpff functions, or c-functions (Stumpff 1959, Equation (V; 43)),

$$c_n(x) = \frac{1}{n!} - \frac{x}{(n+2)!} + \frac{x^2}{(n+4)!} - \ldots; \quad n = 0, 1, 2, \ldots. \tag{12}$$

Note that Gauss's f and g functions and those given in Equations (9) and (10) have different individual terms, but the overall structure is the same (see Section 3.3). For the problems studied here, an initial guess s_0 for s based on Equation (18) in Danby (1987) worked well in `orbitN`:

$$s_0 = \frac{1}{r}\,\tau - \frac{\chi}{2r^3}\,\tau^2. \tag{13}$$

Because the Stumpff functions are based on a series expansion, the series may be truncated at lower n for small x, given a required accuracy (say, machine precision). For planetary systems with a large range in x, the integrator performance can thus be improved by reducing n depending on x; a simple option to do so is available in `orbitN`. The primary choice to solve Kepler's equation is usually based on the Newton–Raphson method (fast and generally accurate), which is also the case in `orbitN`. As a secondary choice (in case Newton–Raphson fails), the secant method (e.g., Danby 1988) was implemented in `orbitN`. As a third and final choice, the bisection method is used (Rein & Tamayo 2015).

3.3. Kahan Compensated Summation

To reduce numerical round-off errors, Kahan compensated summation (operator $\mathcal{S}$, see Section 3) was implemented in `orbitN` (Kahan 1965). At least two different implementation options are possible: (1) $\mathcal{S}$ is applied after each operation that updates the state variables, say, $[\boldsymbol{x}_j\ \boldsymbol{v}_j]_{t+\tau} = [\boldsymbol{x}_j\ \boldsymbol{v}_j]_t + [\Delta\boldsymbol{x}_j\ \Delta\boldsymbol{v}_j]$, i.e., multiple times per time step Δt. (2) $\mathcal{S}$ is applied only once per time step, and the incremental updates from different operators during Δt are accumulated into a separate set of variables ($\delta\boldsymbol{x}_j$, $\delta\boldsymbol{v}_j$), representing changes in state variables, to which $\mathcal{S}$ is applied. The advantage of option 1 is that carrying ($\delta\boldsymbol{x}_j$, $\delta\boldsymbol{v}_j$) through the integration is avoided; its disadvantage is that $\mathcal{S}$ has to be applied multiple times per time step. The advantage of option 2 is that $\mathcal{S}$ has to be applied only once per time step; its disadvantage is that ($\delta\boldsymbol{x}_j$, $\delta\boldsymbol{v}_j$) has to be carried through the integration. Furthermore, internally, the updated sum ($\boldsymbol{x}_j + \delta\boldsymbol{x}_j$) and/or ($\boldsymbol{v}_j + \delta\boldsymbol{v}_j$) have to be evaluated during the time step regardless because its value is required as input to a subsequent operator. I tested both options and found no significant differences in results or performance. Option (1) was implemented in `orbitN-1.0`, which adds a computational overhead of about 3% for a full solar system integration.

Kahan compensated summation generally uses increments, say, $(\Delta \boldsymbol{x}, \Delta \boldsymbol{v})$, and hence is straightforward to apply following the Kick operator because accelerations, $\boldsymbol{a}$, and $\Delta \boldsymbol{v} = \boldsymbol{a} \times \tau$ are explicitly calculated in the Kick routine. However, the Drift operator uses f and g functions (Equations (9) and (10)) to advance $(\boldsymbol{x}, \boldsymbol{v})$ for each body from time t to $t + \tau$, which is not expressed in terms of increments:

$$\boldsymbol{x}(t + \tau) = f \cdot \boldsymbol{x}(t) + g \cdot \boldsymbol{v}(t) \tag{14}$$

$$\boldsymbol{v}(t + \tau) = \dot{f} \cdot \boldsymbol{x}(t) + \dot{g} \cdot \boldsymbol{v}(t). \tag{15}$$

As mentioned above, the f and g functions in `orbitN` are adjusted for use with universal variables and Stumpff functions and differ from Gauss's f and g functions, although they have the same structure (see Section 3.2). Inserting Equations (9) and (10) into Equations (14) and (15), the last two equations may be rewritten in terms of $\Delta \boldsymbol{x}$ and $\Delta \boldsymbol{v}$:

$$\Delta \boldsymbol{x} = \widehat{f} \cdot \boldsymbol{x}(t) + g \cdot \boldsymbol{v}(t) \tag{16}$$

$$\Delta \boldsymbol{v} = \dot{f} \cdot \boldsymbol{x}(t) + \widehat{\dot{g}} \cdot \boldsymbol{v}(t), \tag{17}$$

where $\widehat{f} = f - 1$ and $\widehat{\dot{g}} = \dot{g} - 1$ (see also Wisdom 2018, who used an analogous procedure with Gauss's f and g functions).

3.4. Symplectic Correctors

Symplectic correctors remove fluctuations in energy and were implemented up to stage 6 = seventh order, following Wisdom (2006). Stages 2, 4, and 6 are available in `orbitN-1.0` and are applied only at the beginning and end of an integration and when output is requested—hence adding essentially no computational overhead. Plots of relative maximum energy changes indeed suggest reductions by up to two orders of magnitude when including the corrector (stage 6). Interestingly, however, for practical applications over, say, the past 60 Myr or so, symplectic correctors make little difference, as the actual dynamics in terms of orbital eccentricity, mean longitude, etc., are hardly affected over that timescale (see Section 4.1).

3.5. M_0's Quadrupole Moment

The gravitational quadrupole potential due to the dominant/central mass M_0 may be written as

$$\Phi_{J2} = \frac{GM_0}{r} J_2 \, (R_0/r)^2 \, \frac{1}{2}(3\cos^2\theta - 1) \tag{18}$$

$$= \frac{A}{r^3}\left(\frac{3z^2}{r^2} - 1\right), \tag{19}$$

with $A = GM_0 \, J_2 \, R_0^2/2$ and $z = r\cos\theta$ (see below for z's reference frame), where J_2 is M_0's quadrupole moment, R_0 is its effective radius (related to oblateness), and θ is the colatitude angle. Applying the gradient $-\nabla\Phi_{J2}$, the accelerations are given by

$$a_x = 3A\left(\frac{5z^2}{r^2} - 1\right)\frac{x}{r^5}; \quad a_y = 3A\left(\frac{5z^2}{r^2} - 1\right)\frac{y}{r^5};$$

$$a_z = 3A\left(\frac{5z^2}{r^2} - 3\right)\frac{z}{r^5}, \tag{20}$$

as implemented in `orbitN` (macro option `J2`). Importantly, in case of the solar system, the solar quadrupole moment is directed along the solar rotation/symmetry axis, which is about 6° and 7° offset from the invariable plane and ECLIPJ2000, respectively. By default, the quadrupole axis in integration coordinates is directed along the z-axis. Thus, if the initial (Cartesian) coordinates (say, obtained from ephemerides) are specified in a different frame, then the coordinates need to be rotated to account for the offset between that frame and the solar rotation axis (Zeebe 2017).

3.6. Lunar Contribution

For solar system integrations, the Moon may be included as a separate object. Alternatively, the Earth–Moon system may be modeled as a point mass at the Earth–Moon barycenter (EMB), plus an additional effect from the Moon's influence on the net EMB motion via a mean quadrupole potential (`orbitN` macro option `LUNAR`). The quadrupole acceleration term may be written as (Quinn et al. 1991)

$$\boldsymbol{a}_Q = -\frac{3 \, GM_0 \, m_E \, m_L \, R^2}{4 \, (m_E + m_L)^2} \cdot \frac{\boldsymbol{r}}{r^5} \cdot f_L, \tag{21}$$

where indices "E" and "L" signify Earth and lunar, respectively, R is an effective parameter for the Earth–Moon distance, and r is the EMB–Sun distance. The factor f_L is a correction factor that deserves a few comments. Quinn et al. (1991) introduced f_L to account for differences between the actual lunar orbit and their simplified model and set $f_L = 0.9473$. Varadi et al. (2003) revisited the issue and suggested $f_L = 0.8525$, based on a comparison to integrations that resolved the Moon as a separate object. Using $f_L = 0.8525$, Zeebe (2017) showed that integrations with a separate Moon (Bulirsch–Stoer algorithm) and Quinn et al.'s lunar model (symplectic map) virtually agreed to ∼63 Myr in the past (i.e., divergence time $\widehat{\tau}_D \simeq 63$ Myr; see Section 4). This timescale is beyond the solar system's intrinsic predictability limit of ∼50 Myr owing to dynamical chaos, and hence the lunar model is likely sufficient for most applications that do not need to resolve the Moon. The `LUNAR` option was implemented in `orbitN` following Quinn et al. (1991) and Rauch & Hamilton (2002).

3.7. Post-Newtonian Corrections from General Relativity

`orbitN-1.0` includes post-Newtonian corrections from GR due to M_0 (to 1PN order), implemented following ST94. The 1PN Hamiltonian may be written as (Landau & Lifshitz 1971; Saha & Tremaine 1994; Will 2014)

$$\mathcal{H}_{\rm PN} = \frac{1}{c^2}\sum_{j=1}^{J}\left(\frac{\mu_j^2 \, m_j'}{2 \, r_j'^2} - \frac{p_j'^4}{8 \, m_j'^3} - \frac{3 \, \mu_j \, p_j'^2}{2 \, m_j' \, r_j'}\right), \tag{22}$$

where c is the speed of light, $\mu_j = G \cdot \sigma_j$ (see Section 2), m refers to mass, r refers to distance, and p refers to momentum. Primes indicate quantities in Jacobi coordinates.

Note that at the present level of approximation (1PN), the difference between, e.g., Jacobi and bodycentric distances and masses can be ignored. Consider the magnitude of the primary Newtonian potential in Gaussian units at 1 au, $GM_0/r = k^2 M_0/r \simeq 10^{-4}$ au^2 day^{-2}, versus the first term of the 1PN potential (Equation (22)), $k^4 M_0^2/(2c^2 r^2) \simeq 10^{-12}$ au^2 day^{-2}, i.e., a relative 1PN magnitude of about 10^{-8}

(factor $k^2M_0/(2c^2r)$). The relative differences between Jacobi and bodycentric distances, $\Delta r/r$ (and masses $\Delta m/m$), for example, for Mercury and Earth are 0 and $\sim 10^{-7}$ ($\sim 10^{-7}$ and $\sim 10^{-6}$). Such differences would introduce a relative error of $\lesssim 10^{-14}$ with respect to the primary Newtonian potential, far beyond the level of accuracy provided by the 1PN approximation.

The 1PN Hamiltonian (Equation (22)) includes cross-terms between positions and momenta and, as written, does not split conveniently into terms similar to Equation (1). However, ST94 devised a method to accommodate $\mathcal{H}_{\rm PN}$ in a symplectic scheme, which also shows favorable performance in terms of energy, angular momentum, and speed (see Section 4.3). Equation (22) may be rewritten as

$$\mathcal{H}_{\rm PN} = \sum_{j=1}^{J} (\alpha_j \, \mathcal{H}^2_{{\rm Kep},j} + \beta_j / r'^2_j + \gamma_j \, p'^4_j), \tag{23}$$

where $\alpha_j = 3/(2m'_j c^2)$, $\beta_j = -\mu_j^2 m'_j / c^2$, and $\gamma_j = -1/(2m'^3_j c^2)$. The α-term merely leads to a scaling of the time step argument of the Drift operator (see Appendix A), the β-term can be easily accommodated in the Kick operator, and the γ-term can be included as leapfrog operators before and after the Drift step. For the current solar system integrations, the 1PN option as implemented in `orbitN` adds less than $\sim$10% computational overhead.

4. Solar System Chaos

In the following, I present solar system integrations with `orbitN` and other integrator packages to provide insight into the integrator algorithms and solar system chaos. As a chaos indicator, the difference between two orbital solutions i and j may be tracked using the divergence time $\hat{\tau}_D$ (see Zeebe 2017), i.e., the time interval ($\hat{\tau}_D > 0$) after which the maximum absolute difference in Earth's orbital eccentricity ($\max|e_i - e_j|$) irreversibly crosses $\sim$10% of mean e ($\sim 0.028 \times 0.1$; Figure 1). The divergence time $\hat{\tau}_D$ as employed here should not be confused with the Lyapunov time, which is the timescale of exponential divergence of trajectories and is only $\sim$5 Myr for the inner planets. For the solutions discussed here, the divergence of trajectories is ultimately dominated by exponential growth, which is indicative of chaotic behavior ($t \gtrsim 40$ Myr for standard solar system integrations; see Section 4.1). Thus, $\hat{\tau}_D$ is largely controlled by the Lyapunov time, although the two are different quantities. Integration errors usually grow polynomially and typically dominate for $t \lesssim 40$ Myr (see, e.g., Figure 1 and Varadi et al. 2003).

4.1. Standard Test: Past 100 Myr

For the present standard solar system integrations, initial conditions for the positions and velocities of the planets and Pluto were generated from the JPL DE431 ephemeris (Folkner et al. 2014),[3] using the SPICE toolkit for Matlab.[4] We have recently also tested the latest JPL ephemeris DE441 (Park et al. 2021), which makes little difference for practical applications because the divergence time relative to the astronomical solution ZB18a (based on DE431) is $\sim$66 Ma (see Section 4.2) and hence beyond ZB18a's reliability limit of $\sim$58 Ma (based on geologic data; see below). The standard integration includes 10 asteroids[5] (for a list of asteroids, see Zeebe 2017). Coordinates were obtained at JD 2,451,545.0 in the ECLIPJ2000 reference frame and subsequently rotated to account for the solar quadrupole moment (J_2) alignment with the solar rotation axis (Zeebe 2017). Our astronomical solutions are provided over the time interval from 100 to 0 Ma. However, as only the interval 58–0 Ma is constrained by geologic data (Zeebe & Lourens 2019), we caution that the interval prior to 58 Ma is unconstrained owing to solar system chaos. The standard integration includes the solar quadrupole moment $J_2 = 1.305 \times 10^{-7}$, the lunar contribution, and 1PN corrections. Unless stated otherwise, the integration time step is $\Delta t = 2$ days, as previously used in our astronomical solution ZB18a (see Section 4.2), which also properly resolves Mercury's pericenter (at eccentricity $\lesssim$0.2), hence avoiding numerical chaos (see Wisdom 2015; Hernandez et al. 2022).

As a first test, the long-term behavior of changes in energy ($\Delta E/E = (E - E_0)/E_0$), angular momentum ($\Delta L_z/L$), and the implementation of Kahan compensated summation and symplectic correctors in `orbitN` is examined (Figure 1). As should be expected from a symplectic algorithm, $|\Delta E/E|$ remains small ($|\Delta L_z/L|$ as well) and does not exhibit any significant trends over 100 Myr. Omitting Kahan summation, maximum $|\Delta E/E|$ and $|\Delta L_z/L|$ increase by up to a factor of $\sim$10. Omitting the symplectic corrector (stage 6 = seventh order; see Wisdom 2006), the energy fluctuations that are removed by the corrector become apparent; the corrector has little effect on $|\Delta L_z/L|$. Omitting both Kahan summation and the corrector yields similar results to omitting just the corrector. The consequences for the dynamics of the system may be illustrated by examining the differences in the EMB's orbital eccentricity (Δe) and mean longitude ($\Delta\lambda$), relative to the standard run (Figures 1(c) and (d)). The effects of Kahan summation and the corrector on Δe are similar to those of a small perturbation or a small difference in initial conditions, which grows over time (see below and Zeebe 2015a, 2015b, 2017). Notably, for practical applications in astrochronology over, say, the past 60 Myr or so, Kahan summation and symplectic correctors would actually make little difference because the divergence time to the standard solution is $\gtrsim$70 Ma (Figure 1(c)), i.e., significantly beyond its reliability limit of $\sim$58 Ma (see above).

4.2. Astronomical Solution ZB18a

The astronomical solution ZB18a was originally obtained with the integrator package `HNBody` (Rauch & Hamilton 2002; `v1.0.10`) using the same setup as described above and the symplectic integrator (second-order WH map) with Jacobi coordinates (Zeebe & Lourens 2019, 2022).[6] In order to lend confidence to the accuracy and reproducibility of long-term orbital solutions for the solar system, it is imperative to compare the new standard solution obtained with `orbitN` (Section 4.1) to the original solution ZB18a (Figure 2). The changes in $|\Delta E/E|$ and $|\Delta L_z/L|$ across the 100 Myr integration with `orbitN` and `HNBody` remain below $\sim 1 \times 10^{-11}$ and $\sim 3 \times 10^{-12}$ throughout the integrations.

The divergence time $\hat{\tau}_D$ for Earth's orbital eccentricity is $\sim$77 Ma (Figure 2(c)), again far beyond the reliability limit of

[3] naif.jpl.nasa.gov/pub/naif/generic_kernels/spk/planets
[4] naif.jpl.nasa.gov/naif/toolkit.html
[5] Initial conditions generated at ssd.jpl.nasa.gov/x/spk.html.
[6] Earth's orbital eccentricity for the ZB18a solution is available at www2.hawaii.edu/~zeebe/Astro.html and www.ncdc.noaa.gov/paleo/study/35174.

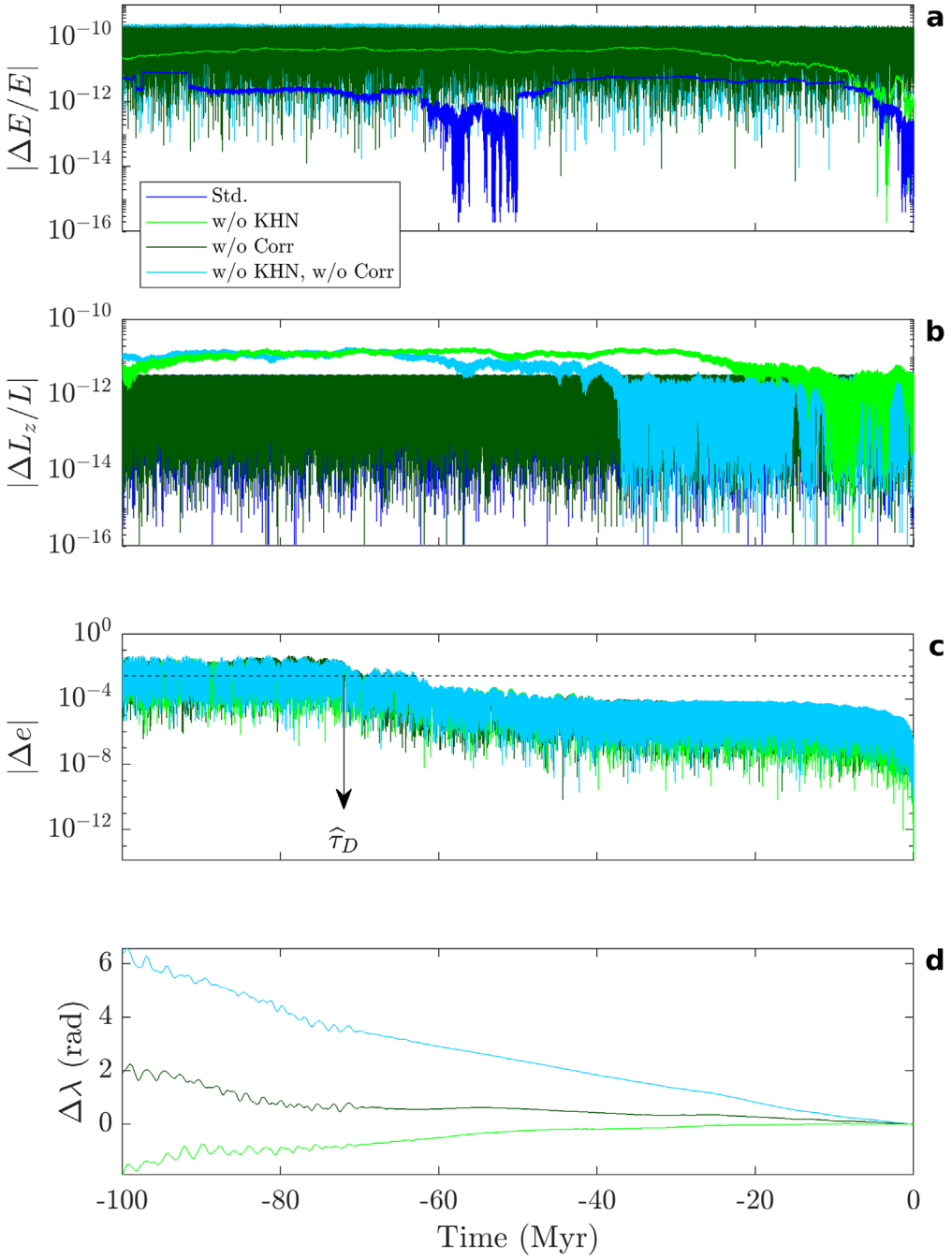

Figure 1. Solar system integrations over the past 100 Myr with `orbitN`. The standard setup (Std.) includes the planets, Pluto, 10 asteroids, J_2, a lunar contribution, and 1PN corrections implemented following Saha & Tremaine (1994). KHN = Kahan compensated summation (Kahan 1965). Corr = symplectic corrector (stage 6 = seventh order; see Wisdom 2006). The time step is $\Delta t = 2$ days. $\Delta E/E = (E - E_0)/E_0$ and $\Delta L_z/L$ indicate relative changes in energy and angular momentum, respectively. Differences in orbital eccentricity (Δe) and mean longitude ($\Delta\lambda$) are for the Earth–Moon barycenter, relative to the standard run. $\widehat{\tau}_D$ is the divergence time (see text).

~58 Ma. $\widehat{\tau}_D \simeq 77$ Ma even exceeds the ~72 Ma calculated for including and excluding Kahan summation and symplectic correctors in a single integrator (`orbitN`, Figure 1), suggesting that, within the limits of the current physical model of the solar system, the performances of the integrators `orbitN` and `HNBody` are very similar.

4.3. Implementation of General Relativity

As mentioned above, `orbitN` includes post-Newtonian corrections from GR due to M_0 (to 1PN order), implemented following ST94 (see Section 3.7), which also applies to `HNBody`. However, other methods of implementing 1PN corrections are possible. For example, the integrator package `REBOUNDx` provides 1PN implementation options such as "`gr_potential`" (Nobili & Roxburgh 1986) and "`gr`" based on a first-order splitting (Tamayo et al. 2020). The option `gr_potential` represents a simplified $1/r^2$ perturbing potential, supposed to mimic the secular advance of perihelia from GR, as proposed by Nobili & Roxburgh (1986), who considered one out of three GR terms and ignored the other two GR terms that are small for the outer planets. The $1/r^2$ potential is known to incorrectly predict, for instance, the instantaneous

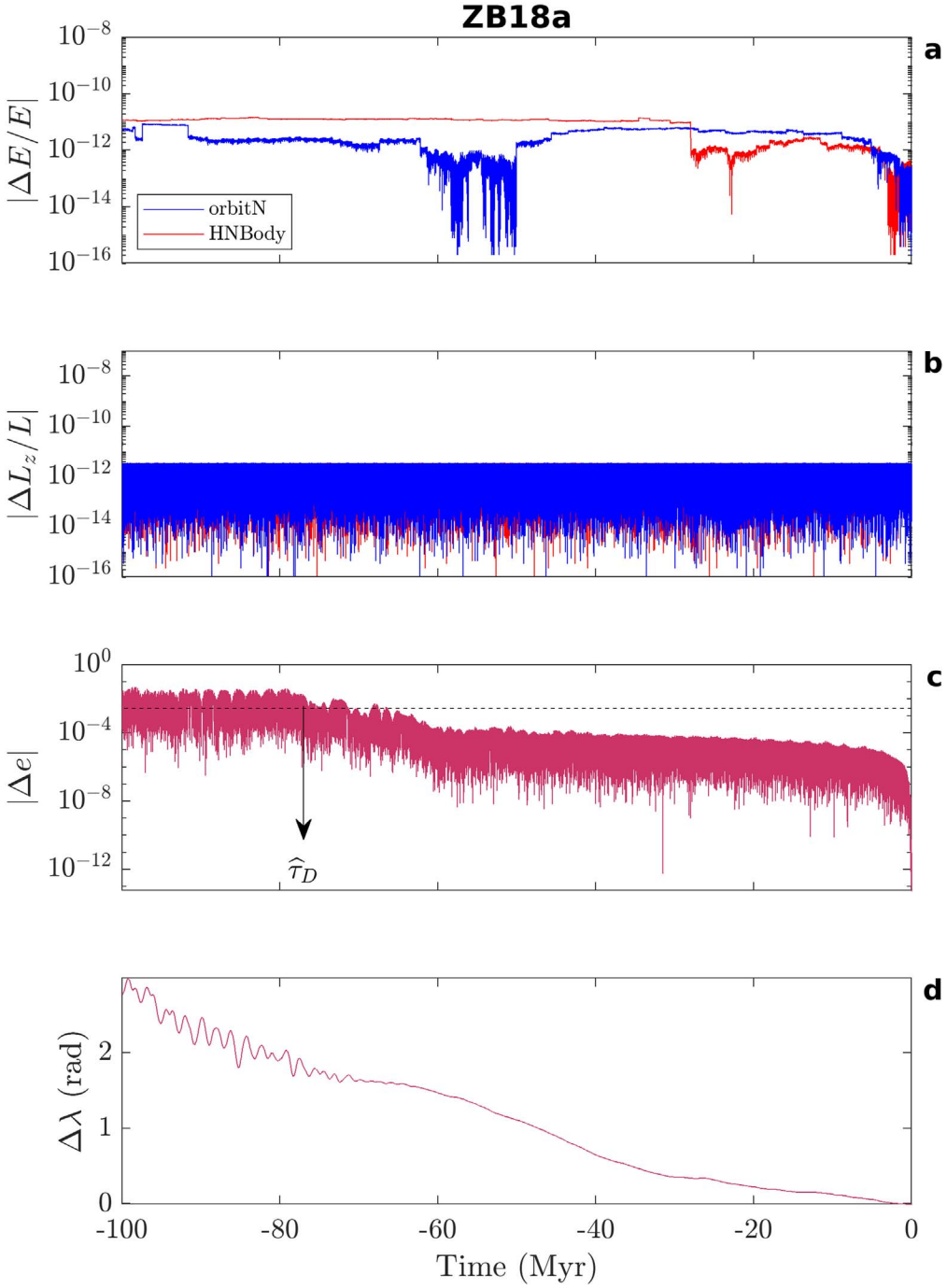

Figure 2. Comparison of solar system integrations with `orbitN` and `HNBody` for the setup of the astronomical solution ZB18a (Zeebe & Lourens 2019; see text for details). $\Delta E/E = (E - E_0)/E_0$ and $\Delta L_z/L$ indicate relative changes in energy and angular momentum, respectively. Differences in orbital eccentricity (Δe) and mean longitude ($\Delta\lambda$) are for the Earth–Moon barycenter. $\widehat{\tau}_D$ is the divergence time (see text).

elements. The option `gr` is more accurate but computationally expensive (see below). It turned out that ST94's method is either more accurate or significantly faster than the `REBOUNDx` GR options. This is not a criticism of the `REBOUNDx` package, or the WH map as implemented in the `REBOUND` package (Rein & Tamayo 2015). Indeed, both packages and their source code availability are very useful, including for developing and testing `orbitN-1.0`. The first-order split 1PN implementation in `REBOUNDx` had a specific intention (for details, see Tamayo et al. 2020) and is likely appropriate for many applications. However, when `gr` is combined with the WH map, for instance, auxiliary computations are required to integrate across the GR step, which results in a significant performance hit. For the user with a specific problem at hand, it seems important to be aware of the differences between various options available in different integrator packages and their characteristics, which may otherwise take a significant effort to figure out.

Regarding performance, it is noteworthy that the 1PN option (ST94) in `orbitN` and `HNBody` adds less than ∼10% computational overhead for the current application, while the `gr_potential` and `gr (+RK2)` options add ∼4% and

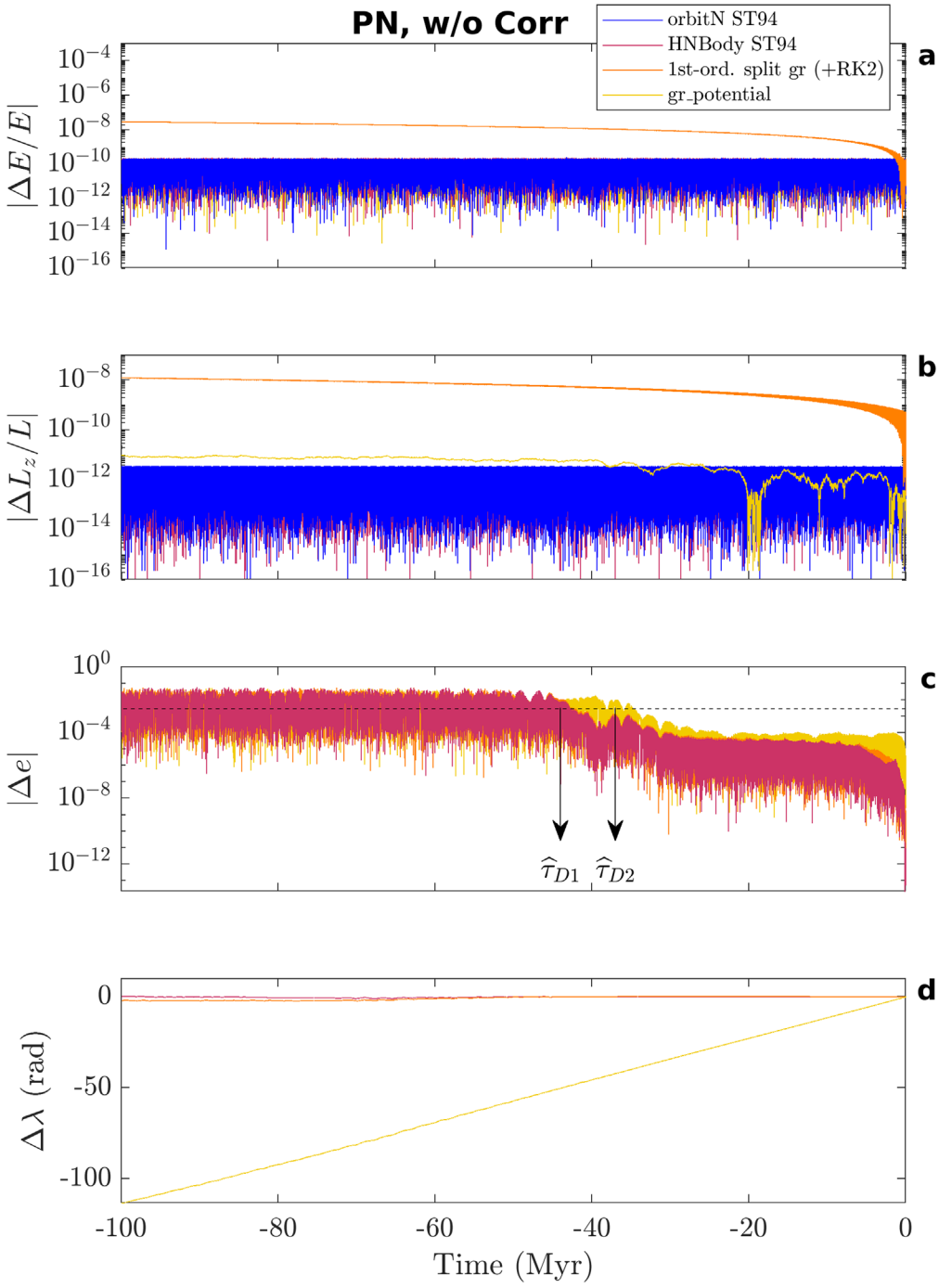

Figure 3. Comparison of solar system integrations with `orbitN`, `HNBody`, and `REBOUND` and different 1PN implementations (see text). The standard setup (Section 4.1) is used, except that in all packages J_2, the lunar contribution (where available), and symplectic correctors are turned off. $\Delta E/E = (E - E_0)/E_0$ and $\Delta L_z/L$ indicate relative changes in energy and angular momentum, respectively. Differences in orbital eccentricity (Δe) and mean longitude ($\Delta\lambda$) are for the Earth–Moon barycenter. $\widehat{\tau}_D$ are divergence times (see text).

∼190% overhead, respectively. Overall, for the 1PN runs displayed in Figure 3, `orbitN` was faster than the `gr` (`+RK2`) option by a factor of ∼2.6. Furthermore, `orbitN` was about as fast as (Intel i9-12900 @2.40GHz) or ∼15% faster than (Intel i5-10600 @3.30GHz) `HNBody v1.0.10`, hence depending on hardware. All tests were performed on 64-bit Linux machines and `gcc` optimization level 3 for `orbitN` and `REBOUND`.

To facilitate a basic comparison, the standard solar system integration setup (Section 4.1) with a few modifications was run in `orbitN`, `HNBody`, and `REBOUNDx` (Figure 3). In all packages, 1PN corrections were turned on, while J_2, the lunar contribution (where available), and symplectic correctors were turned off. In `orbitN` the 1PN energy contribution was calculated according to Equation (22), while in `REBOUNDx` the functions `rebx_gr_potential_potential()` and `rebx_gr_hamiltonian()` were used. In `orbitN`, the 1PN angular momentum was calculated following Poisson & Will (2014), while in `REBOUNDx` no equivalent function seems available. In `HNBody`, routines for 1PN energy and angular

momentum have apparently been coded (likely similar to those in orbitN, as can be inferred from the output), but the details are unavailable because the source code is inaccessible.

The results for $|\Delta E/E|$ and $|\Delta L_z/L|$ computed with orbitN and HNBody (both follow ST94's 1PN implementation) are virtually identical, while $|\Delta E/E|$ and $|\Delta L_z/L|$ (for $t \lesssim -5$ Myr) increase linearly for the gr option (see Figure 3; note logarithmic ordinate). The differences in the 1PN implementations also affect the orbital dynamics, showing significant differences in the EMB's orbital eccentricity and mean longitude for gr_potential, while the gr results are closer to those of orbitN (Figures 3(c) and (d)). The divergence time $\hat{\tau}_{D1} \simeq 44$ Myr for the difference in the EMB's orbital eccentricity (Δe) between orbitN and HNBody (Figure 3(c)) is typical for runs with 1PN corrections enabled but J_2 and the lunar contribution disabled (see Section 4.4). However, the corresponding $\hat{\tau}_{D2} \simeq 37$ Myr between orbitN and gr_potential is distinctly shorter. Thus, it appears that the numerical 1PN implementation can enhance the apparent chaos in the system.

Then, how can one distinguish between numerical and physical effects on the system's dynamics and apparent chaoticity? In other words, how can one tell whether one solution is more accurate than another? In the present case, the known limitations of gr_potential suggest that ST94's method is more accurate, as illustrated by differences in the EMB's orbital eccentricity and mean longitude (see Figures 3(c) and (d)). However, $|\Delta E/E|$ and $|\Delta L_z/L|$ do not hint at problems with the gr_potential method, as long as $|\Delta E/E|$ is calculated within the framework of the $1/r^2$ perturbing potential (see Figures 3(a) and (b)). Conversely, $|\Delta E/E|$ and $|\Delta L_z/L|$ for the gr option may raise a red flag, yet the calculated EMB's orbital eccentricity and mean longitude are closer to those of ST94's method. Testing divergence times of integrators for the same perturbation can also provide some insight to distinguish between methods (see Section 4.4). Further indications may be obtained by applying a different integrator algorithm to the same problem. For example, Zeebe (2017) showed that solar system integrations with HNBody but fundamentally different algorithms (nonsymplectic Bulirsch–Stoer method vs. the symplectic WH map, both 1PN enabled) virtually agree to ∼63 Myr in the past, although this observation says more about the basic algorithms than the 1PN implementation. Thus, in summary, inspection of $|\Delta E/E|$ and $|\Delta L_z/L|$, as well as prior knowledge and additional tests, can assist in finding suitable criteria to distinguish between numerical and physical effects on the system's apparent chaoticity. However, identifying such criteria is not straightforward in the present case and can be even trickier in other cases.

4.4. J_2, Lunar, and PN Effects on Chaos

In the following, I use orbitN to provide insight into the effect of various physical processes on the long-term chaos in the solar system, including GR (PN), J_2 (J2), and the lunar contribution (LUN). For the standard setup ZB18a (see Section 4.2), the different physical effects were turned on and off in various combinations, and for each combination ensemble runs were performed ($K = 16$), with Earth's initial x-coordinate perturbed by $\Delta x_0^k = k \times 10^{-12}$ au ($k = 0,\ldots, K-1$). Note that $\Delta x_0 = 10^{-12}$ au is much smaller than the difference in x_0, say, between different ephemerides such as DE431 and INPOP13c ($\Delta x_0 \simeq 10^{-9}$ au; Zeebe 2017). Next, $\hat{\tau}_D$ was determined for each ensemble member relative to the respective reference run ($k = 0$). The purpose of the above procedure is to examine the evolution of a small perturbation under the solar system's chaotic dynamics and measure the exponential divergence of trajectories (using $\hat{\tau}_D$) for different physical effects. Tendentially, the smaller $\hat{\tau}_D$, the stronger the chaos. The ensembles provide some insight into the system's multitude of solutions for a set of initial conditions and allow identifying exceptional runs (see below).

Turning on only PN gives the smallest $\hat{\tau}_D$ of about 40 Myr (+PN −J2 −LUN; green diamonds in Figure 4). Adding J2 stabilizes somewhat (green triangles), yet removing PN has an even more stabilizing effect (blue diamonds), increasing $\hat{\tau}_D$ to ∼60–70 Myr (−PN −J2 −LUN; Figure 4). Note that the run with $\hat{\tau}_D \simeq 100$ Myr ($k = 9$; blue diamond, arrow) is not an error or "outlier" that can therefore be excluded (the run was carefully examined). The run is a proper solution of the system, illustrating the inherent unpredictability of chaotic systems and their unaccountability in terms of conventional statistics. The effect of adding the lunar contribution (−PN −J2 +LUN; blue triangles in Figure 4) increases $\hat{\tau}_D$ from 60–70 Myr to $\gtrsim$70 Myr. The possible causes behind these effects, as well as the different PN implementations (Section 4.3) in relation to the chaos in the system, are discussed below considering the system's fundamental frequencies (Section 4.5).

4.5. Changes in Fundamental Frequencies

Several resonances and their overlap have been proposed and investigated as the cause of the chaos in the solar system, including the $2(g_4 - g_3) - (s_4 - s_3)$ resonance and the interaction between g_5 (largely Jupiter's forcing frequency) and g_1 as part of the $(g_1 - g_5) - (s_1 - s_2)$ resonance (Laskar 1990; Sussman & Wisdom 1992; Ito & Tanikawa 2002; Morbidelli 2002; Lithwick & Wu 2011; Batygin et al. 2015; Zeebe 2017; Mogavero & Laskar 2022; Zeebe 2022; Brown & Rein 2023). The g and s frequencies (aka fundamental, or secular frequencies, eigenmodes, etc.) are constant in quasi-periodic systems but vary over time in chaotic systems, although some combinations, such as $(g_2 - g_5)$, are more stable than others (for discussion, see, e.g., Spalding et al. 2018). It is critical to recall that there is no simple 1-to-1 relationship between planet and eigenmode, particularly for the inner planets. The system's motion is a superposition of all eigenmodes, although some modes represent the single dominant term for some (mostly outer) planets. The $g_1 - g_5$ interaction, "$(g_1 - g_5)$" for short, can force Mercury's eccentricity to high values and plays a critical role in the long-term stability of the solar system on a Gyr timescale (e.g., Laskar 1990; Batygin & Laughlin 2008; Lithwick & Wu 2011; Zeebe 2015a; Abbot et al. 2023; Brown & Rein 2023). Importantly, $(g_1 - g_5)$ is affected by GR, as PN corrections move g_1 up (by $\sim 0\farcs43\ \mathrm{yr}^{-1}$ at present) and away from g_5 (for illustration, see Figure 4 in Zeebe 2015a), thus reducing the tendency for instability on a Gyr timescale.

On the contrary, PN corrections increase chaoticity (decrease the divergence time) in the current 100 Myr simulations (compare blue and green diamonds in Figure 4), suggesting that other mechanisms, for example, the $2(g_4 - g_3) - (s_4 - s_3)$ resonance, may be more important on a 100 Myr timescale. Indeed, spectral analysis of, for instance, the present integrations comparing the first-order split and the symplectic 1PN implementation (cf. Figure 3) reveal differences in g_3 and g_4

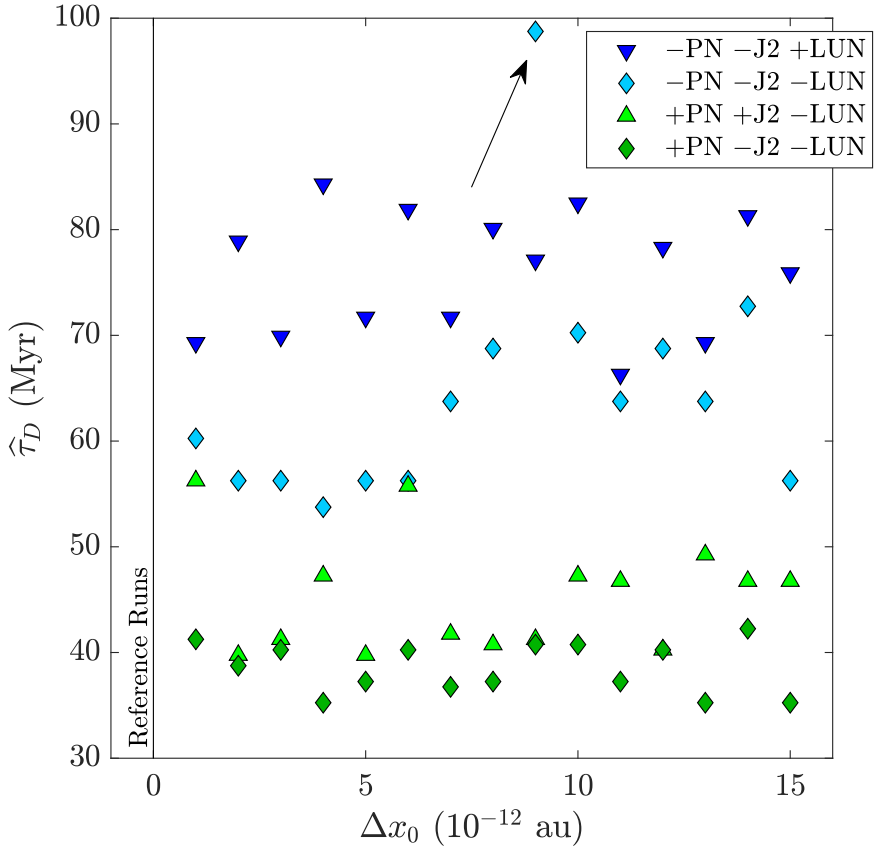

Figure 4. Ensemble integrations with `orbitN` turning on/off (+/ −) GR (`PN`), J_2 (`J2`), and the lunar contribution (`LUN`) in different combinations. Earth's initial x-coordinate is perturbed by Δx_0, relative to the corresponding reference run ($\Delta x_0 = 0$ au). $\hat{\tau}_D$ is the divergence time (see text).

(see Figure 5), as well as small differences in s_3 and s_4 (not shown), consistent with a recent analysis of variations in Earth's and Mars's orbital inclination and obliquity across the same timescale (Zeebe 2022). Presuming that different resonances dominate on different timescales suggests a potential mechanism for GR corrections having opposite effects on a Gyr versus 100 Myr timescale, say, through $(g_1 - g_5)$ versus $(g_4 - g_3)$. As mentioned above, GR moves up g_1 and away from g_5 (the shift is much larger for g_1 than for g_5 and $g_1 > g_5$). GR also moves up g_3 and g_4, and the shift is also (somewhat) larger for g_3 than for g_4—however, in this case $g_3 < g_4$. In this oversimplification, GR would hence increase $(g_1 - g_5)$ but decrease $(g_4 - g_3)$. While this notion appears consistent with the results of the integrations performed here (summarized in Figure 4), spectral analysis of selected runs suggests a much more complex pattern, as detailed in the following. Below, spectra are presented based on the fast Fourier transform (FFT), which was used to extract the fundamental frequencies (g and s) from the classic variables:

$$h = e\sin(\varpi) \quad ; \quad k = e\cos(\varpi) \tag{24}$$

$$p = \sin(I/2)\sin\Omega \quad ; \quad q = \sin(I/2)\cos\Omega, \tag{25}$$

where e, I, ϖ, and Ω are eccentricity, inclination, longitude of perihelion, and longitude of ascending node, respectively.

For the two-body problem, the change in the argument of perihelion, ω, due to GR may be written as (Einstein 1916)

$$\dot{\omega} = 24\pi^3 \frac{a^2}{c^2 T^2 (1 - e^2)} \cdot T^{-1}, \tag{26}$$

where a, e, and T are the semimajor axis, eccentricity, and orbital period, respectively; c is the speed of light; and the factor T^{-1} yields $\dot{\omega}$ per unit time (instead of per orbit). Equation (26) gives $\dot{\omega} \simeq 0\farcs43$, $0\farcs038$, and $0\farcs014\ \mathrm{yr}^{-1}$ for the orbits of Mercury, Earth, and Mars, respectively, at present. Spectral analysis (−25 to 0 Myr) of runs with and without PN (blue/green diamonds in Figure 4) give a shift of $\Delta g_1 = 0\farcs36\ \mathrm{yr}^{-1}$ (Figure 6(a)), indicating that g_1 reflects Mercury's orbit but not in a simple manner, in which case one would expect $\Delta g_1 = 0\farcs43\ \mathrm{yr}^{-1}$. For the same runs, FFT yields $\Delta g_3 = 0\farcs073\ \mathrm{yr}^{-1}$ and $\Delta g_4 = 0\farcs055\ \mathrm{yr}^{-1}$ (Figure 6(a)), showing large differences to Equation (26) (which predicts $\dot{\omega}$ in a two-body system). Thus, while the FFT analysis shows similar tendencies to Equation (26), the full interacting system is much more complex, as expected. As mentioned above, in general there is no simple 1-to-1 relationship between a single planet and a single eigenmode. Note also the large shift in s_2 (Figure 6(b)).

The stabilizing effect of the lunar contribution (compare blue diamonds and blue triangles in Figure 4) appears similarly convoluted. The change in the argument of perihelion of the Earth–Moon barycenter due to the lunar contribution may be written as (see Equation (21) and Appendix B)

$$\dot{\omega} = \frac{nB}{a^2(1 - e^2)^2} \quad ; \quad B = \frac{3\ m_E\ m_L\ R^2}{4\ (m_E + m_L)^2} \cdot f_L, \tag{27}$$

where n is the mean motion. Equation (27) gives $\dot{\omega} \simeq 0\farcs066\ \mathrm{yr}^{-1}$ for the EMB's orbit at present. Spectral analysis (−25 to

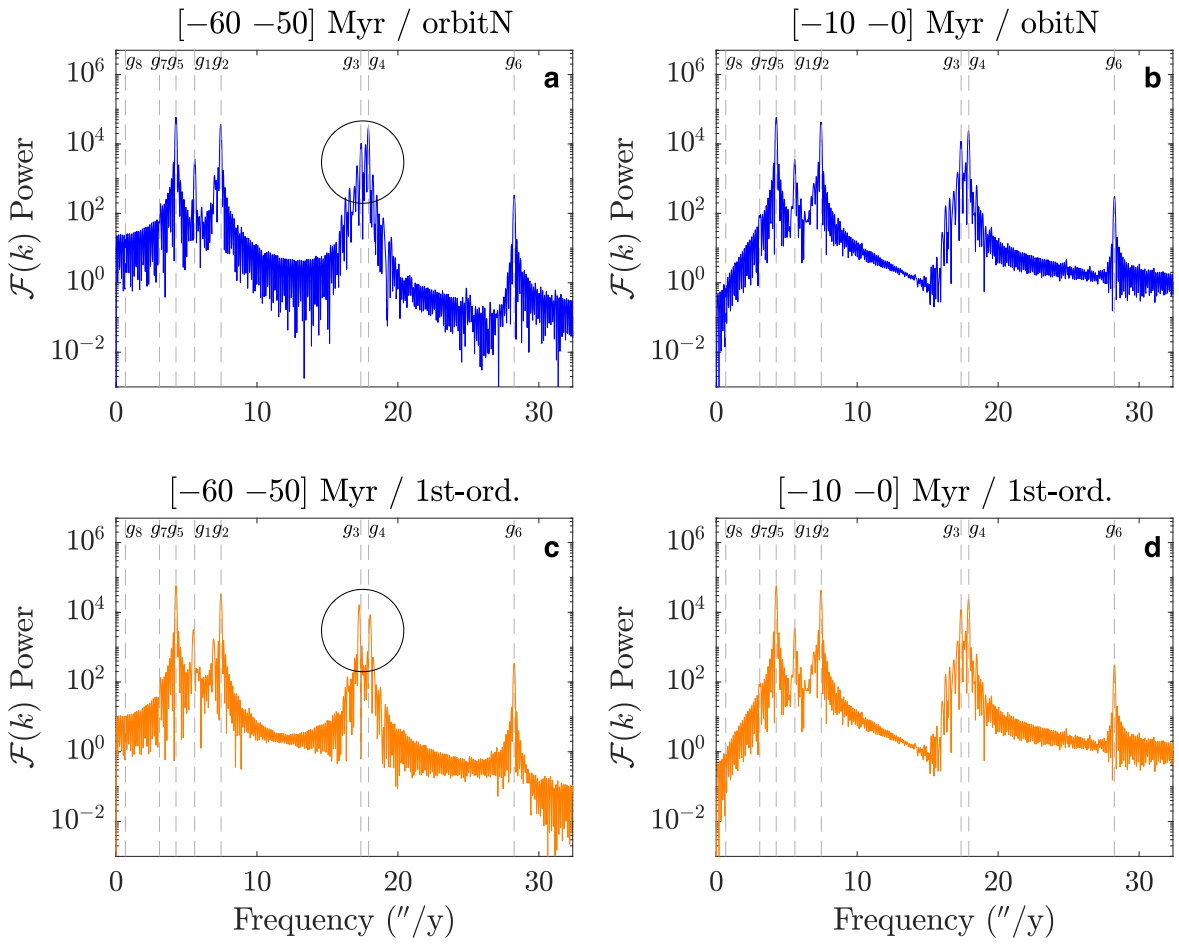

Figure 5. Time series analysis of Earth's $k = e\cos(\varpi)$ (see text) across the intervals −60 to −50 Myr and −10 to 0 Myr to extract solar system g-modes from runs with `orbitN` and `REBOUND gr (+RK2)` for different 1PN implementations (see Figure 3). $\mathcal{F}$ = FFT. Vertical dashed lines indicate frequencies of g-modes (see Zeebe 2017). Note differences in g_3 and g_4 in [−60, −50] Myr (circles in panels (a) and (c)).

0 Myr) of runs with and without `LUN` give a smaller g_3 shift and, in addition, significant shifts in g_1, g_2, and g_4 (Figure 6(c)), as well as sizable shifts in s_1 and s_2 (Figure 6(d)). Note also that the results for Δg_i and Δs_i as presented in Figure 6 depend on the time interval selected for spectral analysis. For example, across the interval −10 to 0 Myr, Δg_2 is actually larger than Δg_3 for the `LUN` on/off case. The numerical values of $2(g_4 - g_3) - (s_4 - s_3)$ and $(g_1 - g_5) - (s_1 - s_2)$ are close to zero for the runs analyzed. In summary, it is clear that while simplified views based on the two-body problem (e.g., Equations (26) and (27)) can be helpful as a starting point, they of course fail to capture the complexity of the long-term dynamics of the full system. Further in-depth analysis of the link between changes in fundamental frequencies, resonances, and chaos may require a detailed eigenmode analysis and signal reconstruction (e.g., Zeebe 2017, 2022), which is beyond the goal of the current paper (that is, to introduce `orbitN`) and is hence left for future work.

5. Summary and Conclusions

I have introduced the symplectic integrator `orbitN` (ver. 1.0) with the primary goal of efficiently generating accurate and reproducible long-term orbital solutions for near-Keplerian planetary systems dominated by a central mass. `orbitN-1.0` is suitable for hierarchical systems without close encounters but can be extended to include additional features in future versions. While the current `orbitN` application focuses on the solar system, `orbitN` can generally be applied to planetary systems with a dominant mass M_0. Among other features, `orbitN-1.0` includes M_0's quadrupole moment, a lunar contribution, and post-Newtonian corrections (1PN) due to M_0 based on a fast symplectic implementation. I have used `orbitN` to provide insight into the effect of various physical processes on the long-term chaos in the solar system. The integrations performed here reveal that 1PN corrections have the opposite effect on chaoticity/stability on a 100 Myr timescale, as compared to a Gyr timescale. Finally, time series analysis was performed to examine the influence of different physical processes on fundamental frequencies, which affect secular resonances and, in turn, the long-term dynamics of the solar system.

I thank David Hernandez and Ilja Kocken for discussions and comments on an earlier version of the manuscript. I also thank the anonymous reviewer for suggestions, which have improved the manuscript. Daniel Tamayo helped clarify 1PN options in `REBOUNDx`. This research was supported by Heising-Simons Foundation grant No. 2021-2800 and U.S. NSF grants OCE20-01022 and OCE20-34660 to R.E.Z.

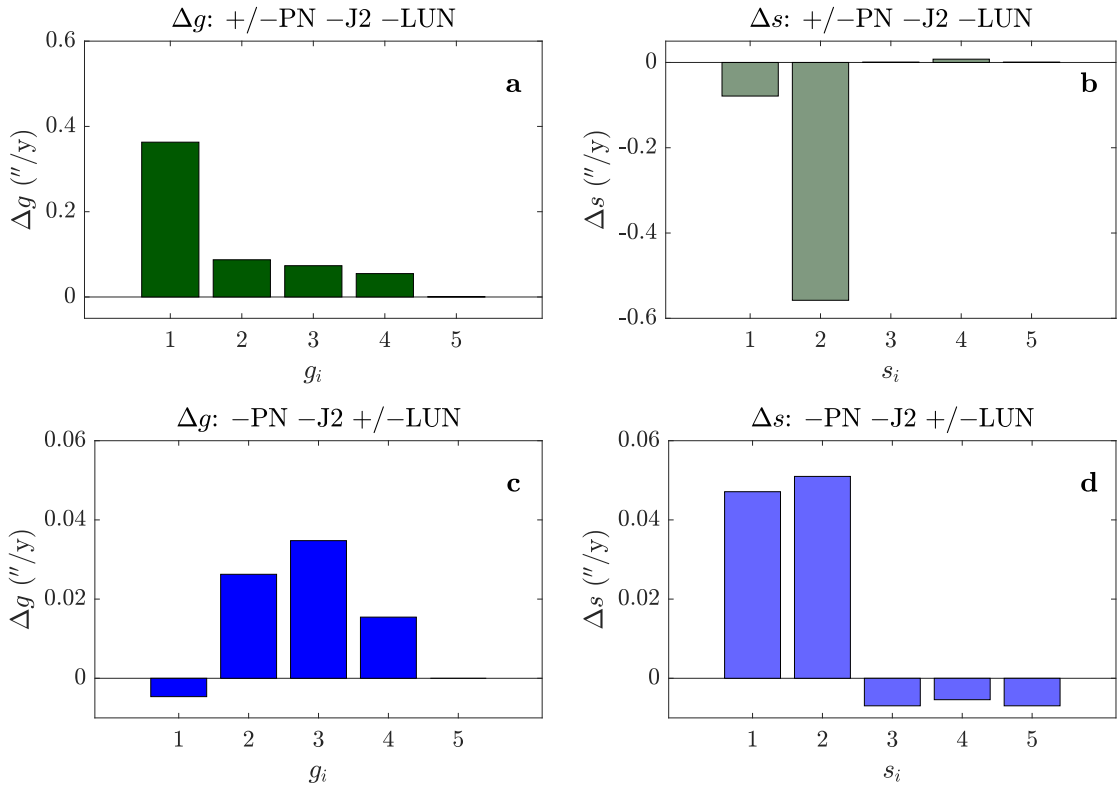

Figure 6. Shifts in fundamental frequencies (Δg_i and Δs_i) from FFT analyses of runs shown in Figure 4 ($\Delta x_0 = 10^{-12}$ au) across the interval −25 to 0 Myr. Shifts are calculated between two runs each with `PN` on/off = +/− (green) and `LUN` on/off = +/− (blue).

Software: `orbitN-1.0` (github.com/rezeebe/orbitN; correspondence to orbitN.code@gmail.com; on Zenodo: Zeebe 2023), `HNBody v1.0.10` (Rauch & Hamilton 2002), `REBOUND v3.19.10` (Rein & Liu 2012; Rein & Tamayo 2015), `REBOUNDx v3.7.1` (Tamayo et al. 2020).

Appendix A
PN: α-term

The term $\alpha_j\ \mathcal{H}^2_{\mathrm{Kep},j}$ in Equation (23) leads to a scaling of the time step argument of the Drift operator (Saha & Tremaine 1994) as detailed in the following. Consider a single body first, i.e., drop index j for the time being. Using Poisson brackets,

$$\{F,\, G\} = \frac{\partial F}{\partial \boldsymbol{x}}\frac{\partial G}{\partial \boldsymbol{p}} - \frac{\partial F}{\partial \boldsymbol{p}}\frac{\partial G}{\partial \boldsymbol{x}}, \tag{A1}$$

Hamilton's equations can be written as ($\boldsymbol{z} = [\boldsymbol{x}\,\boldsymbol{p}]$)

$$\dot{\boldsymbol{z}} = \{\boldsymbol{z},\, \mathcal{H}\} \quad \Rightarrow \quad \dot{\boldsymbol{x}} = \frac{\partial \mathcal{H}}{\partial \boldsymbol{p}} \quad ; \quad \dot{\boldsymbol{p}} = -\frac{\partial \mathcal{H}}{\partial \boldsymbol{x}}. \tag{A2}$$

If $\{\boldsymbol{z},\, \mathcal{H}\} \equiv \mathcal{D}$ is considered an operator acting on $\boldsymbol{z}$, then

$$\dot{\boldsymbol{z}} = \mathcal{D}\,\boldsymbol{z}, \tag{A3}$$

with the formal solution

$$\boldsymbol{z} = \boldsymbol{z}_0\ e^{\tau \mathcal{D}}. \tag{A4}$$

Now let $\mathcal{H} = \mathcal{H}_{\mathrm{Kep}} + \alpha\mathcal{H}^2_{\mathrm{Kep}}$ (only affecting the Drift operator); then,

$$\dot{\boldsymbol{z}} = \{\boldsymbol{z},\, \mathcal{H}_{\mathrm{Kep}} + \alpha\mathcal{H}^2_{\mathrm{Kep}}\} \tag{A5}$$

$$\dot{\boldsymbol{x}} = \frac{\partial \mathcal{H}_{\mathrm{Kep}}}{\partial \boldsymbol{p}}\ (1 + 2\alpha\mathcal{H}_{\mathrm{Kep}}) \tag{A6}$$

$$\dot{\boldsymbol{p}} = -\frac{\partial \mathcal{H}_{\mathrm{Kep}}}{\partial \boldsymbol{q}}\ (1 + 2\alpha\mathcal{H}_{\mathrm{Kep}}). \tag{A7}$$

$\mathcal{H}_{\mathrm{Kep}}$ yields the two-body energy $-\mu m'/2a$, where a is the semimajor axis. Using $\alpha = 3/(2m'c^2)$, it follows $2\alpha\mathcal{H}_{\mathrm{Kep}} = -3\mu/(2c^2 a)$. Finally, we can write

$$\boldsymbol{z} = \boldsymbol{z}_0\ e^{\tau\mathcal{D}\ (1+2\alpha\mathcal{H})} = \boldsymbol{z}_0\ e^{\tau'\mathcal{D}}, \tag{A8}$$

with $\tau' = \tau\ [1 - 3\mu/(2c^2 a)]$. Comparing Equations (A4) and (A8) shows that inclusion of the α-term only changes the time step argument of the Drift operator. Reintroducing the body index j, it follows $\tau'_j = [1 - 3\mu_j/(2c^2 a_j)]$, i.e., τ is scaled for each body individually, depending on mass factor μ_j and semimajor axis a_j.

Appendix B
Lunar Effect on $\dot{\omega}$ of EMB's Orbit

The quadrupole acceleration term due to the lunar contribution may be written as (Equation (21))

$$\boldsymbol{a}_Q = -\mu_0 B \frac{\boldsymbol{r}}{r^5}, \tag{B1}$$

where $\mu_0 = GM_0$ and

$$B = \frac{3\ m_E\ m_L\ R^2}{4\ (m_E + m_L)^2} \cdot f_L\,, \tag{B2}$$

which can be derived from a potential ($\boldsymbol{a}_Q = -\nabla\Phi_Q$)

$$\Phi_Q = -\mu_0 B\frac{1}{3r^3}. \tag{B3}$$

Upon averaging, r^3 may be replaced by $a^3(1-e^2)^{3/2}$. Hence, taking as the disturbing function

$$\mathfrak{R} = \frac{\mu_0 B}{3a^3(1-e^2)^{3/2}}, \tag{B4}$$

$\dot{\omega}$ is given by (Danby 1988; Murray & Dermott 1999)

$$\dot{\omega} = \frac{na\sqrt{1-e^2}}{\mu_0 e}\frac{\partial\mathfrak{R}}{\partial e}, \tag{B5}$$

where n is the mean motion and $\partial\mathfrak{R}/\partial i = 0$ was used (i = inclination). Finally,

$$\dot{\omega} = \frac{nB}{a^2(1-e^2)^2}. \tag{B6}$$

ORCID iDs

Richard E. Zeebe https://orcid.org/0000-0003-0806-8387

References

Abbot, D. S., Hernandez, D. M., Hadden, S., et al. 2023, ApJ, 944, 190
Batygin, K., & Laughlin, G. 2008, ApJ, 683, 1207
Batygin, K., Morbidelli, A., & Holman, M. J. 2015, ApJ, 799, 120
Brown, G., & Rein, H. 2023, MNRAS, 521, 4349
Chambers, J. E. 1999, MNRAS, 304, 793
Danby, J. M. A. 1987, CeMec, 40, 303
Danby, J. M. A. 1988, Fundamentals of Celestial Mechanics (Richmond, VA: Willmann-Bell Inc.)
Duncan, M. J., Levison, H. F., & Lee, M. H. 1998, AJ, 116, 2067
Einstein, A. 1916, AnP, 49, 769
Folkner, W. M., Williams, J. G., Boggs, D. H., Park, R. S., & Kuchynka, P. 2014, IPNPR, 196, 1
Fukushima, T. 1997, CeMDA, 66, 309
Hernandez, D. M., & Dehnen, W. 2017, MNRAS, 468, 2614
Hernandez, D. M., Zeebe, R. E., & Hadden, S. 2022, MNRAS, 510, 4302
2019, IEEE Std 754-2019 (Revision of IEEE 754-2008) (New York: IEEE), 1
Ito, T., & Kojima, S. 2005, PNAOJ, 8, 17
Ito, T., & Tanikawa, K. 2002, MNRAS, 336, 483
Kahan, W. 1965, Communications of the ACM, 8, 40
Kaufmann, D. E. 2005, Swifter—an Improved Solar System Integration Software Package, www.boulder.swri.edu/swifter
Landau, L., & Lifshitz, E. 1971, The Classical Theory of Fields (Oxford: Pergamon)
Laskar, J. 1990, Icar, 88, 266
Laskar, J., Fienga, A., Gastineau, M., & Manche, H. 2011, A&A, 532, A89
Levison, H. F., & Duncan, M. J. 1994, Icar, 108, 18
Lithwick, Y., & Wu, Y. 2011, ApJ, 739, 17
Mikkola, S. 1997, CeMDA, 67, 145
Mikkola, S., & Aarseth, S. J. 1998, NewA, 3, 309
Mikkola, S., & Innanen, K. 1999, CeMDA, 74, 59
Mogavero, F., & Laskar, J. 2022, A&A, 662, L3
Morbidelli, A. 2002, Modern Celestial Mechanics: Aspects of Solar System Dynamics (London: Taylor and Francis)
Murray, C. D., & Dermott, S. F. 1999, Solar System Dynamics (Cambridge: Cambridge Univ. Press), 592
Nobili, A., & Roxburgh, I. W. 1986, in Relativity in Celestial Mechanics and Astrometry. High Precision Dynamical Theories and Observational Verifications, ed. J. Kovalevsky & V. A. Brumberg, Vol. 114 (Dordrecht: Springer), 105
Park, R. S., Folkner, W. M., Williams, J. G., & Boggs, D. H. 2021, AJ, 161, 105
Poisson, E., & Will, C. M. 2014, Gravity: Newtonian, Post-Newtonian, Relativistic (Cambridge: Cambridge Univ. Press), 780
Quinn, T. R., Tremaine, S., & Duncan, M. 1991, AJ, 101, 2287
Rauch, K. P., & Hamilton, D. P. 2002, BAAS, AAS/Division of Dynamical Astronomy Meeting #33, 34, 938
Rauch, K. P., & Holman, M. 1999, AJ, 117, 1087
Rein, H., & Liu, S. F. 2012, A&A, 537, A128
Rein, H., & Tamayo, D. 2015, MNRAS, 452, 376
Saha, P., & Tremaine, S. 1994, AJ, 108, 1962
Spalding, C., Fischer, W. W., & Laughlin, G. 2018, ApJL, 869, L19
Stiefel, E. L., & Scheifele, G. 1975, Linear and Regular Celestial Mechanics (Berlin: Springer)
Stumpff, K. 1959, Himmelsmechanik. Bd. 1: Das Zweikörperproblem und die Methoden der Bahnbestimmung der Planeten und Kometen (Berlin: Deutscher Verlag der Wissenschaften)
Sussman, G. J., & Wisdom, J. 1992, Sci, 257, 56
Tamayo, D., Rein, H., Shi, P., & Hernandez, D. M. 2020, MNRAS, 491, 2885
Varadi, F., Runnegar, B., & Ghil, M. 2003, ApJ, 592, 620
Will, C. M. 2014, PhRvD, 89, 044043
Wisdom, J. 2006, AJ, 131, 2294
Wisdom, J. 2015, AJ, 150, 127
Wisdom, J. 2018, MNRAS, 474, 3273
Wisdom, J., & Holman, M. 1991, AJ, 102, 1528
Wisdom, J., & Holman, M. 1992, AJ, 104, 2022
Yoshida, H. 1990, PhLA, 150, 262
Zeebe, R. E. 2015a, ApJ, 798, 8
Zeebe, R. E. 2015b, ApJ, 811, 9
Zeebe, R. E. 2017, AJ, 154, 193
Zeebe, R. E. 2022, AJ, 164, 107
Zeebe, R. E. 2023, orbitN: A Symplectic Integrator for Near-Keplerian Planetary Systems, Version 0.5.0, Zenodo, doi:10.5281/zenodo.7933000
Zeebe, R. E., & Lourens, L. J. 2019, Sci, 365, 926
Zeebe, R. E., & Lourens, L. J. 2022, E&PSL, 592, 117595